Boost of the Bio-memristor Performance for Artificial Electronic Synapses by Surface Reconstruction

Jingjuan Wang,[#1] Chenyang Shi,[#2,3] Maria L. Sushko,[4] Jinling Lan,[1] Kaixuan Sun,[1] Jianhui Zhao,[1] XiangYang Liu,*[5] Xiaobing Yan,*[1]

[1] *Key Laboratory of Brain-Like Neuromorphic Devices and Systems of Hebei Province, College of Electron and Information Engineering, Hebei University, Baoding 071002, China*

[2] *Department of Chemistry, University of Washington, Seattle, Washington 98195, United States*

[3] *Research Institute for Biomimetics and Soft Matter, College of Materials, Fujian Provincial Key Laboratory for Soft Functional Materials Research, Xiamen University, Xiamen 361005, China.*

[4] *Physical and Computational Sciences Directorate, Pacific Northwest National Laboratory, Richland, Washington 99352, United States*

[5] *College of Ocean and Earth Sciences, State Key Laboratory of Marine Environmental Science (MEL) , Xiamen University, Xiamen 361005, China.*

[#] *Jingjuan Wang, Chenyang Shi equally contributed to this paper.*

**Correspondence should be addressed to X.B.Y. (email: yanxiaobing@ime.ac.cn) or to X.Y.L.(liuxy@xmu.edu.cn)*

ABSTRACT

Biomaterials-based memristor (bio-Memristor) are often adopted to emulate biological synapses functions and applied to construct neural computing networks in brain inspired chip systems. However, the randomness of conductive filament formation in bio-memristor inhibits their switching performance by causing the dispersion in of the device-switching parameters. In this case, a facile porous silk fibroin (SF)-memristor were obtained through protein surface reconstruction strategy, in which the size of pore can be adjusted by the density of hybrid nano seeds. The porous SF-memristor exhibit greatly enhanced electrical characteristics, including uniform *I–V* cycles, centralized distribution of the switching voltages, and both high and low resistances, compared to those of devices with without pores. The results of three-dimensional (3D) simulations based on classical density functional theory (cDFT) suggest that reconstructed pores in SF layers guides the formation and fracture of Ag filaments under electric field and enhance the overall conductivity by separating Ag^+ and electron diffusion pathways. Ag^+ are predicted to preferentially diffuses through pores, while electrons diffuse through SF network. Interestingly, the device conductance can be bidirectional modulated gradually by positive and negative voltage and can vividly simulate short-term plasticity, long-term plasticity and even realize the triplet-spike-timing dependent plasticity (triplet-STDP) rule which can be used to pattern recognition in biological systems. The simulation results reveal that a memristor network of this type has the accuracy of

memory learning ~95.78% and the capability of pattern learning. This work provides a facile technology route to improve the performance of bionic-material Memristor.

KEYWORDS: Bio-Memristor; porous modulation; silk fibroin; Artificial Synapses; Surface Reconstruction

INTRODUCTION

Memristor is considered to be one of the fundamental passive circuit elements, which are side by side with resistor, inductor and capacitor. As its name suggests, a memristor combines the properties of resistance and memory, meaning that its resistance depends on the current and voltage signal transmission process it previously participated in. Memristor has been widely studied in the field of memory and logic application.[1-3] Especially, it is an attractive candidate for simulating synaptic functions in biological nervous systems and neural network. The computational structure of a neural morphology can simulate the learning, memory function and perception ability similar to human brain, which are accomplished by abundant numbers of neurons $\sim 10^{12}$ and synapses $\sim 10^{15}$.[4] Synaptic plasticity is that synapses regulate the strength of connections between neurons and promote learning and memory.[5] The resistance modulation of memristor is similar to biological synapses that synaptic plasticity can be increased or decreased.[6] Memristor simulation of biological synaptic plasticity is necessary to achieve high precision artificial synapses. The stimulation pattern of spike sequences containing multiple spikes in biological neurons is more common than single spikes or pairs of spikes. This is due to the spike information sent by different neurons connected to a single neuron can be received.[7] The information contained in spike sequences allows for specific high-level synaptic plasticity, known as spike rate dependent plasticity (SRDP).[8] Bienenstock-Cooper-Munro (BCM) learning rule is an important type of SRDP besides Hebbian learning rules, which describe synaptic modifications that depend on history. In the BCM framework, the high/low spike frequency of the pulse train may lead to the increase/decrease in the synapse weight, depending on whether the spike frequency is higher than the threshold.[9-12] Theoretically, BCM learning rules can be closely replicated using a generic model based on triplet-spike-timing dependent plasticity (triplet-STDP). At present, the development of the BCM rules for memristors is still in its infancy, and the physical mechanisms of memristor operation have yet to be identified.

To achieve high efficiency of artificial synapse memristor, many materials have been reported to be employed as functional medium, including phase-changing materials, ferroelectrics and magnetoelectrics.[13-15] Natural biomaterials possess ideal characteristics for the development of next-generation sustainable electronic products: biocompatibility, biodegradability and so on. Among the few bio-electronic materials, silk fibroin with a self-

tunable property is an excellent candidate material for next-generation flexible and biodegradable electronics.[16] As the most representative protein, it has been investigated to work as medium for artificial synapse memristor devices application.[17-19] However, the existing silk-film based bio-memristor devices are compromised by large switching voltage or dispersion of switching voltages. To overcome this disadvantage, previous work focused on optimizing the performance of the memristor by reconstructing the internal structure of the protein based switching layer.[20] Generally, it is need to introduce additional functional substances, such as metal nanoclusters, carbon nanodots, etc.[21,22] The purpose is to use the change of electric field distribution caused by different surface work functions of these functional materials to induce the formation of uniform and stable conductive filaments, and finally improve the switching performance. However, this functionalization strategy has its drawbacks, such as incomplete biodegradation of the device and cumbersome preparation steps. For biomaterial based memristor, the growth path of conductive filaments often depends on the distributions of the local field strength of the top electrode and the bottom electrode under an applied electric field. Modification of the surface structure such as pattern, hole, triggers the redistribution of the internal electric field. If the local electric field can be optimized through simple surface reconstruction on the mesoscale, and the uniform growth of conductive filaments can be guided, the device performance can be significantly improved. This strategy is called the surface reconstruction strategy. For example, porous films are of the interest for electronic device as they can introduce cone-shaped contact and reduce the dissipation of Joule heat, thus achieving superior electrical performance.[23] It is well known that uncontrollable growth of conductive filament due to a random nature of heterogeneous nucleation will cause the dispersion in switching parameters. In contrast, when a porous silk membrane has a uniform pore distribution, consequently, the Ag dots nucleate in the pores and protrude at the lower surface of the upper electrode, enhancing the localized electrical field and guiding the direction of filament growth. In other words, porous silk film can pre-pave the diffusion path of Ag, effectively minimizing the dispersion of switching-parameters.

In this work, we adopt Bovine Serum Albumin (BSA) as a porogen to prepare porous silk fibroin (p-SF) film as switching layer, and fabricate artificial electronic synapse devices with a p-SF/indium tin oxide (ITO) structure on polyethylene naphthalate (PEN) substrates. We further study the preparation process of porous silk fibroin films and the adjustments of pore size were characterized by using Atomic force microscopy (AFM). The device exhibits a centralized distribution of switching voltages and a slowly varying *I–V* characteristic, thereby realizing the essential functions of single artificial synapses. Three-dimensional (3D) simulations for Ag electrode interfacing nonporous and porous silk fibroin support the hypothesis of pore-directed filament growth. Memristor display basic electrochemical properties, potentiating and depressing conduction, spike-timing-dependent plasticity (STDP),

paired-pulse facilitation (PPF) and the generalized BCM learning rules are demonstrated by the last spike dominated triplet-STDP. In addition, it is confirmed that p-SF is biodegradable and the devices can work normally under mechanical bending. These results illustrate the feasibility of using p-SF film based artificial synapses for neuromorphic systems in detail.

RESULTS AND DISCUSSION

The present of (GAGAGS)n repeats favor SF materials to form stable structure, as they can self-assemble into discrete β-sheet crystallites (β-crystallites). Other proteins, such as BSA, are tend to metastable in helical structure. This difference in crystallization pathway also provides an opportunity for surface engineering of hybrid protein films. To harness the benefits of controllable crystallization process of SF, water-soluble nano-seeds are used as pore-forming agents to simply and reliably prepare SF films with the porous surface structure on the mesoscopic scale. The fabrication process of the porous silk fibroin film with the BSA porogen is shown in Figure 1a. On the basis of Flory-Huggins's lattice model, the 'solute' (the secondary component in mixture: BSA) disperses in a "solvent" (the predominant component: SF). The substrate (ITO) was immersed in a SF/BSA blended solution, and then coated with an SF/BSA hybrid film on the surface of the substrate.[24,25] At the mass ratio of BSA:SF employed in this work (20:80), the BSA phase-separated on the mesoscale, forming uniform aggregates in the hybrid film (Figure 1b). As reported, organic solvents such as glycerol or methanol cause changes in the secondary structure of SF, resulting increased crystallinity and β-sheet content, forming the β-crystallite networks (Figure 1b), rendering the SF materials insoluble in water.[26-28] In this regard, the predominant component (SF) of the hybrid film is insoluble whereas BSA still soluble after glycerol treatment (Figure S1). Therefore, the globulin leached SF film by working as a porogen, which was leached out in water to form the porous film. Atomic force microscopy (AFM) images revealed a highly uniform pore morphology with depths and diameters of 18 ± 5 nm and 120 ± 30 nm, respectively (Figure 1c and 1d). Far-UV circular dichroism (CD) measurement is a common and effective method to study the secondary structure of proteins.[29,30] As shown in Figure 1e, the SF-BSA hybrid film consisted of α-helix (mainly from BSA), which could be confirmed by a maximal positive peak at 192 nm and two typical negative peaks at 210 nm and 222 nm. After the glycerol treatment, the porous film exhibits a significant negative cotton effect around 217 nm, which confirms that the characteristics belongs to the structure of the β-sheet.[29-31]

The morphology of the reconstructed porous p-SF film can be changed by adjusting the ratio of BSA to SF. Figure 2A shows the AFM images of film morphology at different BSA to SF ratios. As shown in Figure 2A-a, the surface morphology of SF/BSA-10 hybrid film displays weak phase separation and the diameter of BSA fusion aggregates of ~ 40 nm. When the density of BSA is 20 wt% or over, strong phase separation occurs as BSA fusion

aggregates reach the diameter of over 120 nm, as shown in Figure 2A-b-e. When the density of BSA in the SF hybrid films reaches 60 wt%, irregular BSA fusion aggregates emerges in the hybrid films (Figure 2A-f). As mentioned before, the globulin leached SF film the way of BSA working as a porogen, which was leached out in water to form the porous film during glycerol post treatment. As shown in Figure 2A-g-k, as the concentration of BSA in the SF film increased from 10 wt% to 50 wt%, the pore size increased from 40 nm to 560 nm due to the fusion of BSA. This increase in pore size implies that morphology of the reconstructed p-SF film is tunable. In addition, both p-SF-10 and p-SF-20 film have highly homogeneous pore size features with obvious nano-/micro-patterns, the pore diameters are concentrated at 40 nm and 130 nm, respectively (Figure S4 (a)-(b)). The final porous films denoted marked as p-SF-10, p-SF-20, p-SF-30, p-SF-40, p-SF-50 and p-SF-60 refer to 10, 20, 30, 40, 50 and 60 wt% of porogen (BSA) in the initial film, respectively. The typical resistive switching behavior of the different p-SF-x devices was investigated. Figures 2B-a-e show the typical bipolar resistive switching behavior of the devices with different BSA to SF ratios in direct current sweep mode at room temperature. These results show that the p-SF-10 and p-SF-20 film devices have highly homogeneous pore size features, more concentrated switching voltage, and excellent cycle durability and stability. And the p-SF-20 film devices are taken as the example to simulate the characteristics of biological synapses.

The mechanism of the resistance switching effect in the p-SF based device is further investigated using electrochemical characterization and cDFT simulations. As shown in Figure S5, the device is stable and uniform, with a narrow range of switching voltages. We speculate that the device performance is improved by the Ag protrusion that forms in the p-SF pores on the lower surface of the Top Electrode (TE). This protrusion, caused by the porous silk film, guides the growth direction of the filament. The creation of Ag protrusion in the pore enhances the strength of local electric field and focuses Ag^+ deposition at the protrusion site as evidenced by Ag^+ ion accumulation in the pore region (Figure 3B) and previous work on memristor devices with a cone-shaped contact [32,33] and on electrochemical deposition on a single-atom protrusion.[34,35] The proposed resistive switching mechanism in Ag/p-SF/ITO is shown in Figure 3A. Restrictive switches are caused by the formation and fracture of conductive Ag filaments. In a fresh Ag/p-SF/ITO device (Figure 3A-a), the filament generates a conductive path in the pores and forms a tip. Unlike the conventional conductive metallic filament mechanism, the filament generates a conductive path in the pores and forms a tip. When a positive voltage is applied to Ag TE, Ag atoms on the electrode are oxidized to Ag^+ ions and flow along the porous path, growing into a conductive filament. The accumulated Ag ions are then reduced to Ag atoms, as shown in Figure 3A-b. The conductivity of Ag filament grows with the increase of applied voltage. Eventually the Ag conductive filaments reach the ITO Bottom Electrode (BE) (Figure 3A-c), and the device will be switches from the HRS to

the LRS. When switching the polarity of the applied electric field, the conductive filaments gradually break off as shown in Figure 3A-d. Consequently, the device resistance rises and the device reverts back to the HRS.

Moreover, to further support the hypothesis confinement-directed filament growth, theoretical simulation of the formation mechanism of filaments in porous films is carried out. 3D theoretical simulations for Ag electrode interfacing nonporous and porous silk fibroin are proposed to support the hypothesis of pore-directed filament growth as shown in Figure 3B. Here, classical density functional theory (cDFT), within the context of the Poisson-Nernst-Planck (PNP) transport kinetics model, was used to model Ag ion and electron diffusion. The model employs a steady state formulation of the PNP. In this formulation, the fluxes J_i for ions and electrons satisfy the Nernst equation (1) coupled to the Poisson equation (3) and the steady state condition (2):

$$-J_i = D_i(r)\left[\nabla\rho_i + \frac{1}{k_BT}\rho_i\left(q_i e\nabla\varphi + \nabla u_i^{id}(r) + \nabla u_i^{ex}(r)\right)\right] \quad (1)$$

$$\nabla J_i = 0 \quad (2)$$

$$-\nabla(\varepsilon(r)\nabla\varphi) = 4\pi\left(\rho_f(r) + e\sum i q_i\rho_i\right) \quad (3)$$

In these equations $D_i(r)$ and ρ_i are the diffusion coefficients and densities of all the species, respectively, φ is the electrostatic potential, $\mu_i^{id}$and $\mu_i^{ex}$are the ideal and excess chemical potential, respectively, $\rho_f(r)$ is the fixed charge density in the system (if any), k_BT is the thermal energy and e is the electron charge. Index "i" denotes mobile species type, e.g. for Ag/solution interface i=1 corresponds to Ag^+, i=2 to e^- and i=3 to water molecules. The supplementary information shows the detailed theoretical model. According to the simulation results, in the absence of pores, ion and electron transport are uniform across planes parallel to the electrode/SF interface and are strongly correlated as shown in Figure 3B-a-c. In contrast, when nanopores are present, the spatial separation of ion and electron diffusion pathways is observed: Ag^+ preferentially diffuses through the pores and electrons through the SF network as shown in Figure 3B-d-f. This spatial separation of electronic and ionic transport is known to lead to higher overall conductivity[36] as it reduces charge recombination and hinders potential reduction in the interfacial region due to the formation of a space-charge layer. The predicted Ag ion accumulation in the pore region at Ag/solution interface suggests that the porous medium guides the formation and fracture of Ag filaments in the device. It also enhances the electron strength in the silk film between the Ag and ITO electrodes, enabling the fast assemblage and breakage of the conductive filaments. This will provide a solution for the speed and uniformity of Memristor. Moreover, the conduction mechanism can be further explained by fitting I-V characteristics based on the above physical mechanism. As

shown in Figure 3C-b, the data at HRS I-V region in the of Ag/p-SF/ITO device in Figure 3C-a can be fitted as ln (I/V^2) versus 1/V.[37-40] The fitting results show the linear behavior at high and low electric field, which points to the F-N tunnel conduction model and the direct tunnel conduction mechanism, respectively. Figure 3C-c shows that the slope of log (I) - log (V) is about 1, which suggests that the device has outstanding ohmic characteristics. The observed effect is consistent with voltage-induced change in gap distance between Ag clusters, that can lead to the gradual tunneling resistance variation emulating biological synaptic function.[3]

Excellent resistive switching properties were further demonstrated by the monotonic increase in conductivity when consecutive positive voltage (0 to 0.2 V) is applied to the device, as shown in Figure 4a. Conversely, the conductivity decreases continuously when a continuous negative (0 to -0.2 V) voltage sweep is applied onto the device (Figure 4b). To clarify this trend, the temporal current and voltage changes in pulse mode are plotted in Figure 4c. Here, we first applied a string of 20 positive voltage pulses (2 V, 250 ns) and then 20 negative pulses (–2 V, 250 ns). Linear conductivity modulation is the ideal method for the back-propagation learning algorithm of Deep Neural Network (DNN), which uses memory as vector matrix multiplication accelerator for pattern processing.[35] Both the potentiation and depression stages were linearly regulated over a wide range. The conductivity increased and decreased under a continuous positive and negative pulse stimulation as shown in Figure 4c, and Figure 4d verifies the cycling stability of the linear regulation. It is noted that the last enhanced conductance is almost equal to the first suppressed conductance, which is considered to facilitate highly controllable and predictable learning processes without the help of cumbersome peripheral circuits. To further verify the successful modulation of device conductance, we applied sequential triangular and sine-wave voltages to the device, and confirmed continuous control of the conductance (Figure 4e and 4f). Obviously, the device conduction was continuously adjustable under positive and negative pulse voltages, which indicates that the response after enhanced or inhibited stimulation is a regulation of synaptic weight. These results indicate that the device is similar to biological synapses.

Furthermore, a triplet-STDP investigation is carried out. Triplet-STDP means that a third spike, either presynaptic or postsynaptic, is introduced into the standard pair-STDP.[41-43] The triplet-STDP reflected the inevitable spike pair interaction in natural spike trains through the short-term inhibition of preceding spikes.[44] The triplet-STDP rule can be used to modify the synaptic weights and other neural simulation dynamic processes, and the memristor based on the triplet-STDP rule can also be implemented. Theoretically, BCM learning rules can be closely replicated using the generalized model based on triplet-STDP.[45] As shown in Figure 5, the suppression triplet-STDP can also be faithfully implemented in the p-SF memristor. Figure 5a-b illustrate two typical triplet sequences. The LTD process (orange) of "post-pre-

post" triplet is induced by the first pairing ("post-pre", $\Delta t_1 < 0$), followed by the second spike pairing("pre-post", $\Delta t_2 > 0$) caused by an LTP process (green), as shown in Figure 5a. Hereafter, the pair (Δt_1, Δt_2) is used to denote the spike timing in triplets and the "post-pre-post" triplet always has the timing of $\Delta t_1 < 0$ and $\Delta t_2 > 0$. For the "pre-post-pre" triplet, Figure 5b shows that the LTP process is activated before the LTD process and the "pre-post-pre" triplet has the timing of $\Delta t_1 > 0$ and $\Delta t_2 < 0$. In the triplet-STDP scheme, each spike applied on the memristor consists of a pair of pulses [V^+/V^- =1 V/−1 V, 100 ns]. Figure 5c-d summarize the data of the last-spike-dominating triplet-STDP with varying Δt_1 and Δt_2 using a colored background to show ΔG. In addition to the "post-pre-post" and "pre-post-pre" modes of the triplet-STDP schematic diagram, there are four other modes (i.e., the pre-spikes (post-spikes) occur before and after a single post-peak (pre-spike)), as shown in quadrants I and III of Figure 5c-d. Similar to the LTP process of paired STDP, the potentiation effect is observed in I quadrant because the pre-spike is always applied before the post-spike regardless of the number of spikes. On the contrary, the quadrants III are similar to the LTD process of paired-STDP, and the pre-spike is always applied after the post-spike, so the depression phenomenon is always observed regardless of the number of spikes. The synaptic weight G in the quadrants II and IV can be switched from depression to potentiation by adjusting the timing of Δt_1 and Δt_2. This proves that the p-SF memristor can successfully simulate the BCM rules by using the triplet-STDP, which has a potential application value in high-order spatiotemporal pattern recognition.

The spiking neuron network connects 108 pre-neurons with one post neuron through synapses and each pre-neuron corresponds to one pixel in the pattern, as shown in Figure 6a. The learning ability of 6×6 pixel predefined pattern memory arrays is simulated using STDP characteristics. Pre-neurons resemble the retina and emit peaks corresponding to visual patterns. In reality, the sensor perceives the mode and immediately reflect the perceived information to the post neuron layer. Random learning method is adopted herein, [46] predefined neurons are alternately activated by pre-determined patterns and noises after each learning, as shown Figure 6b. First, we randomly define the starting value of synaptic weight, with a 50% probability of pattern and noise, respectively, and the noise contains two randomly distributed pixels. The simulation results show that the more times you learn, the closer you approach the ideal pattern, as shown in Figure 6. With the increase in the number of learning times, the learning accuracy rapidly improves until it reaches a saturated state and starts fluctuating near the saturation value as shown in Figure 6d. The learning performance accuracy can be expressed as follows:

$$\text{Accuracy} = [1 - \sqrt{\sum_{i=1}^{n} \frac{(G_t(i) - G_i(i))^2}{n}}] \times 100\% \quad (4)$$

Where $G_t(i)$ and $G_i(i)$ are the target and learned conductance of the i_{th} synapse in a system with n synapses; Figure 6d shows that the accuracy of learning reaches 95.78%. Notably, noise plays a randomizing role in the learning process.

Finally, the solubility and flexibility of porous silk fibroin membranes were further studied. The controllable biodegradability of Ag/p-SF/ITO device is shown in a papain solution (5 mg mL^{-1}) as shown in Figure 7a. The device can be dissolved in papain solution within 10 minutes, which means that the Ag/p-SF/ITO device is well biodegradable.[47,48] Then the flexibility of the Ag/p-SF/ITO devices are tested and Figure 7b shows the flexibility of the device. Figure 7c shows five recorded I-V logarithmic curves under the bending lengths are 13 mm, 11 mm, 9 mm, 7mm, and flat, respectively. The HRS and LRS variations under different bending lengths as shown in Figure 7d. It is observed that there are no obvious fluctuations of I-V curves and resistances in the range of bending conditions, which shows that the device has excellent stability even in bended state. The analysis of the effects of repeated bending on device resistance shows that even after bending 1000 times the ratio of resistance of HRS and LRS remains unchanged, which proves that the device has excellent stability (Figure 7e). Overall, these results demonstrate the potential of p-SF-based devices for implantable biomedical devices and biodegradable devices.

CONCLUSIONS

In summary, porous silk film can be fabricated using the strategy of mesoscopic morphology reconstruction, to optimized memristor performance including device mechanical and cycling stability, and uniform switching characteristics. Accordingly, the reconstructed silk memristor can fully emulate the excitation and inhibition of bio-logical synapses, i.e., the gradual enhancement and inhibition of conduction under the action of positive and negative pulses. Furthermore, the memristor device faithfully mimicked the learning and memory functions of synapses, including using a generic model based on triplet-STDP to implement BCM learning rules. The learning ability of memristor network was verified by stochastic mode learning. The 3D simulation results predict that the Ag^+ ions preferential diffuses through the pores while electrons through the SF network, facilitating the formation and dissolution of the conductive filaments in confinement. In addition, the porous silk memristor is inherently biodegradable and flexible, these unique features of the reconstructed silk memristor makes it a promising device for potential applications in sustainable data storage, synthetic neural networks, and other biocompatible and biodegradable electronics. This work provides an effective strategy for fabricating bio devices with relatively uniform switching parameters and behavior that mimics bio-synapses.

EXPERIMENTAL SECTION

Materials: Buy BSA powder, sodium bicarbonate, lithium bromide from Aladdin (Shanghai, China). Glycerol was obtained from Sinopharm Chemical Reagent. Silk fibroin (SF) solution

was prepared as previously reported.[28,49] Sericin was extracted from silkworm cocoon by frequent stirring and boiling with 0.5% sodium bicarbonate for 60 minutes. The extracted silk was washed and dried at 40 °C for 12 h. Then extracted silk were dissolved in 9.3 mol L^{-1} LiBr solution at 60 °C for 4 h and then the deionized water was dialyzed with cellulose tube (molecular weight cut-off of 3500D) to remove LiBr for 2 d, and 7% w/v solution was obtained. SF solution was mixed with BSA solution. Briefly, BSA solution at 25 mg/mL was added to SF solutions at weight ratios: 20:80.

Device Fabrication: The substrate (ITO) was immersed in a SF/BSA blended solution, and then coated at speed 0.1 mm/s. In post treatment procedure, the hybird film was incubated in glycerol solution at room temperature for 24 hours, then rinse in deionized water to removed glycerol and BSA and dried for 12 h. Then the Ag electrodes with diameter of 90μm and thickness of 70 nm were grown by mask.

Simulation： Simulations were performed using atomistic-to-mesoscale classical density functional theory / Poisson-Nernst-Planck formalism for many-body correlated dynamics in complex heterogeneous environment[50] to study ambipolar Ag^+ and electron transport at the interface of Ag electrode and porous or non-porous SF matrix. The interface is characterized by the dielectric discontinuity with dielectric constant changing from over 78 in the solution phase and metal electrode to 2 in the SF matrix. The model of the porous SF contained a cylindrical pore normal to Ag electrode partially filled with Ag metal (see Figure 3B-b). The pore diameter was 20 nm. The model treats the electric potential driven diffusion process using steady-state dynamics, in which, Ag^+ and electron driven by the gradient in chemical potentials, diffuse in the solvent and hop between the electron acceptor sites on the SF, respectively. Chemical potentials are calculated using a parameter-free approach that couples elementary diffusion processes and mesoscale correlated fluctuation dynamics. The total chemical potential of the system includes the Coulomb electrostatic, many-body electrostatic correlation, excluded volume and chemical short-range, e.g. energy cost for elementary diffusive hops.

Characterization: The secondary structures of protein film were determined by a CD spectra, which was collected on a Jasco 715 model spectropolarimeter. AFM (Veeco Multi Mode 8) used the Tapping mode in the air. Direct current measurements were performed in the atmosphere using a digital source table (keithley 2400). The input of the front and rear spikes is achieved using two pulse channels of Keithley 4225 PMU and 4225 RPM, respectively. Pulse waveforms before and after the measurement were collected by an oscilloscope (LeCroy62mxs-b). In electrical measurement, voltage bias affects the top electrode and the bottom electrode remains grounded.

SUPPLEMENTARY MATERIAL

See the supplementary material for Figs. S1–S11 and Tables S1. We also include information about the classical density functional theory simulations method.

AUTHORS' CONTRIBUTIONS

X.Y. and X.L. conceived and designed the research. J.W. and C.S. conducted characterizations and electrochemical measurements. M.S. performed cDFT calculations. J.L., K.S., and J.Z. added the experimental data. All authors discussed and analyzed the data. X.Y., X.L., J.W., C.S. co-wrote the manuscript.

ACKNOWLEDGEMENT

This work was financially supported by the National Natural Science Foundation of China (grant nos. 61674050 and 61874158), the Project of Distinguished Young of Hebei Province (grant no. A2018201231), the Support Program for the Top Young Talents of Hebei Province (Grant No. 70280011807), the Hundred Persons Plan of Hebei Province (grant nos. E2018050004 and E2018050003), the Supporting Plan for 100 Excellent Innovative Talents in Colleges and Universities of Hebei Province (grant no. SLRC2019018), Special project of strategic leading science and technology of Chinese Academy of Sciences (grant no. XDB44000000-7), outstanding young scientific research and innovation team of Hebei University , Special support funds for national high level talents (grant nos. 041500120001 and 521000981426), Hebei University graduate innovation funding project in 2021(grant no. HBU2021bs013), One of the authors, X.-Y. Liu's primary affiliation is Department of Physics, National University of Singapore." This work was financially supported by NUS AcRF Tier 1 (R-144-000-367-112), 111 project (B16029), and the 1000 Talents Program funding from the Xiamen University. Theoretical simulations were performed at Pacific Northwest National Laboratory (PNNL) with support from the U.S. Department of Energy, Office of Science, Basic Energy Sciences, Division of Materials Sciences and Engineering, under Award KC020105 - FWP12152. PNNL is operated by Battelle for the Department of Energy under Contract No. DE-AC05-76RLO1830.

REFERENCES

1. Xia, Q.; & Yang; J. J. Memristive Crossbar Arrays for Brain-inspired Computing. *Nat. mater*. 2019, 18, 309-323.
2. Yan, X.; Pei, Y.; Chen, H.; Zhao, J.; Zhou, Z.; Wang, H.; Zhang, L.; Wang, J.; Li, X.; Qin, C.; Wang, G.; Xiao, Z., Zhao, Q.; Wang, K.; Li, H.; Ren, D., Liu, Q.; Zhou, H.; Chen, J.& Zhou, P. Self-Assembled Networked PbS Distribution Quantum Dots for Resistive Switching and Artificial Synapse Performance Boost of Memristor. *Adv. Mat*. 2019, 31, 1805284.
3. Zhang, J., Yang, T., Wang, J., Zhao, J., & Yan, X. Memristive device with highly continuous conduction modulation and its underlying physical mechanism for electronic synapse application. Sci. China. Mater. 2021, 64, 179-188.
4. Park, Y.; & Lee, J. S. Artificial Synapses with Short- and Long-Term Memory for Spiking Neural Networks Based on Renewable Materials. *ACS nano*. 2017, 11, 8962-8969.
5. Kuzum, D.; Yu, S.; & Wong, H. P. Synaptic Electronics: Materials, Devices and Applications. *Nanotechnology*. 2013, 24, 382001.
6. Xing, Y.; Shi, C.; Zhao, J.; Qiu, W.; Lin, N.; Wang, J.; Yan, X., Yu, D., Liu, X. Mesoscopic-Functionalization of Silk Fibroin with Gold Nanoclusters Mediated by Keratin and Bioinspired Silk Synapse. *Small*. 2017, 13, 1702390.
7. De La Rocha, J., Doiron, B.; Shea-Brown, E.; Josić, K.; & Reyes, A. Correlation Between Neural Spike Trains Increases with Firing Rate. *Nature*, 2007, 448, 802-806.
8. Sjöström, P. J.; Turrigiano, G. G.; & Nelson, S. B. Rate, Timing, and Cooperativity Jointly Determine Cortical Synaptic Plasticity. *Neuron*. 2001, 32, 1149-1164.
9. Kirkwood, A.; Rioult, M. G.; & Bear, M. F. Experience-Dependent Modification of Synaptic Plasticity in Visual Cortex. *Nature*, 1996, 381, 526-528.
10. Bear, M. F.; Cooper, L. N.; & Ebner, F. F. A Physiological Basis for A Theory of Synapse Modification. *Science*, 1987, 237, 42-48.
11. Cooper, L. N.; & Bear, M. F. The BCM Theory of Synapse Modification at 30: Interaction of Theory with Experiment. *Nat. Rev. Neurosci*. 2012, 13, 798-810.
12. Zenke, F.; Agnes, E. J.; & Gerstner, W. Diverse Synaptic Plasticity Mechanisms Orchestrated to Form and Retrieve Memories in Spiking Neural Networks. *Nat. Commun.* 2015, 6, 1-13.
13. Kuzum, D.; Jeyasingh, R. G.; Lee, B., & Wong; H. S. P. Nanoelectronic Programmable Synapses Based on Phase Change Materials for Brain-Inspired Computing. *Nano. Lett*. 2011, 12, 2179-2186.
14. Guo, R.; Lin, W.; Yan, X. B.; Venkatesan, T.; & Chen, J. Ferroic Tunnel Junctions and Their Application in Neuromorphic Networks. *Appl. Phys. Rev*. 2020, 7, 011304.
15. Sheng, Y.; Edmonds, K. W.; Ma, X.; Zheng, H.; & Wang, K. Adjustable Current-Induced

Magnetization Switching Utilizing Interlayer Exchange Coupling. *Adv. Electron. Mater*. 2018, 4, 1800224.

16. Mukherjee, C.; Hota, M. K.; Naskar, D.; Kundu, S. C.; & Maiti, C. K. Resistive Switching in Natural Silk Fibroin Protein-based Bio-Memristor. *Phys. Status. Solidi. A*. 2013, 210, 1797-1805.
17. Zhu, B.; Wang, H.; Leow, W. R.; Cai, Y.; Loh, X. J.; Han, M. Y.; Chen, X. Silk Fibroin for Flexible Electronic Devices. *Adv. Mater*. 2018, 28, 4250-4265.
18. Hota, M. K.; Bera, M. K.; Kundu, B.; Kundu, S. C.; Maiti, C. K. A Natural Silk Fibroin Protein-Based Transparent Bio-Memristor. *Adv. Funct. Mater*. 2012, 22, 4493-4499.
19. Amsden, J. J.; Domachuk, P.; Gopinath, A.; White, R. D.; Negro, L. D.; Kaplan, D. L.; Omenetto, F. G. Rapid nanoimprinting of silk fibroin films for biophotonic applications. *Adv. Mater*. 2010, 22, 1746-1749.
20. Shi, C.; Wang, J.; Sushko, M. L.; Qiu, W.; Yan, X. B.; & Liu, X. Y. Silk Flexible Electronics: From Bombyx mori Silk Ag Nanoclusters Hybrid Materials to Mesoscopic Memristor and Synaptic Emulators. *Adv. Funct. Mater*. 2019, 29, 1904777.
21. Zhao, Q.; Xie, Z.; Peng, Y. P.; Wang, K.; Wang, H. D.; Li, X. N., Wang, H. W.; Chen, J. S.; Zhang, H.; Yan, X. Y. Current Status and Prospects of Memristor Based on Novel 2D Materials. *Mater. Horiz*. 2020, 7, 1495-1518.
22. Yan, X. B.; Wang, K.; Zhao, J.; Zhou, Z.; Wang, H.; Wang, J.; Pei, Y. A New Memristor with 2D Ti3C2Tx MXene Flakes as an Artificial Bio-Synapse. *Small*, 2019, 15, 1900107.
23. Ling, H.; Yi, M., Nagai; M., Xie, L.; Wang, L.; Hu, B.; Huang, W. Controllable Organic Resistive Switching Achieved by One-Step Integration of Cone-Shaped Contact. *Adv. Mater*. 2017, 29, 1701333.
24. Hu, X.; Cebe, P.; Weiss, A. S.; Omenetto, F.; Kaplan, D. L. Protein-based Composite Materials. *Mater. Today*. 2012, 15, 208-215.
25. Prum, R. O.; Dufresne, E. R.; Quinn, T.; Waters, K. Development of Colour-Producing β-Keratin Nanostructures in Avian Feather Barbs. *J. R. Soc. Interface*. 2009, 6(suppl_2), S253-S265.
26. Brown, J. E.; Davidowski, S. K.; Xu, D.; Cebe, P.; Onofrei, D.; Holland, G. P.; Kaplan, D. L. Thermal and Structural Properties of Silk Biomaterials Plasticized by Glycerol. *Biomacromolecules*. 2016, 17, 3911-3921.
27. Lu, S.; Wang, X.; Lu, Q.; Zhang, X.; Kluge, J. A.; Uppal, N.; Kaplan, D. L. Insoluble and Flexible Silk Films Containing Glycerol. *Biomacromolecules*. 2009, 11, 143-150.
28. Tu, H.; Yu, R.; Lin, Z., Zhang; L., Lin, N.; Yu, W. D.; Liu, X. Y. Programing Performance of Wool Keratin and Silk Fibroin Composite Materials by Mesoscopic Molecular Network Reconstruction. *Adv. Funct. Mater*. 2016, 26, 9032-9043.
29. Bai, S.; Liu, S.; Zhang, C.; Xu, W.; Lu, Q.; Han, H.; Zhu, H. Controllable Transition of

Silk Fibroin Nanostructures: an Insight into in Vitro Silk Self-Assembly Process. *Acta. Biomater*. 2013, 9, 7806-7813.

30. Lu, S.; Li, J.; Zhang, S.; Yin, Z.; Xing, T.; Kaplan, D. L. The Influence of the Hydrophilic-Lipophilic Environment on the Structure of Silk Fibroin Protein. *J. Mater. Chem. B*. 2015, 3, 2599-2606.
31. Canetti, M.; Seves, A.; Secundo, F.; Vecchio, G. CD and Small-Angle X-ray Scattering of Silk Fibroin in Solution. Biopolymers: *Original Research on Biomolecules*. 1989, 28, 1613-1624.
32. Ling, H., Yi, M., Nagai, M., Xie, L., Wang, L., Hu, B., & Huang, W. Controllable Organic Resistive Switching Achieved by One-Step Integration of Cone-Shaped Contact. Adv. Mater. 2017, 29, 1701333.
33. Sun, Y., Song, C., Yin, J., Chen, X., Wan, Q., Zeng, F., & Pan, F. Guiding the Growth of A Conductive Filament by Nanoindentation to Improve Resistive Switching. ACS appl. Mater. Inter. 2017, 9, 34064-34070.
34. Ding, F., Xu, W., Graff, G. L., Zhang, J., Sushko, Maria. L., Chen, X., Shao, Y., Engelhard, M. H., Nie, Z., Xiao, J., Liu, X., Sushko, P. V., Liu, J., and Zhang, J. Dendrite-free Lithium Deposition via Self-healing Electrostatic Shield Mechanism. J. Am. Chem. Soc. 2013, 135, 4450-4456.
35. Liu, Q.; Long, S.; Lv, H.; Wang, W.; Niu, J.; Huo, Z. L.; Chen, J. N.; Liu, M. Controllable Growth of Nanoscale Conductive Filaments in Solid-Electrolyte-based ReRAM by Using a Metal Nanocrystal Covered Bottom Electrode. *ACS Nano*, 2010, 4, 6162-6168.
36. Yu, J.; Sushko, M. L.; Kerisit, S.; Rosso, K. M.; & Liu, J. Kinetic Monte Carlo Study of Ambipolar Lithium Ion and Electron–Polaron Diffusion into Nanostructured TiO_2. *J. Phys. Chem. Lett*. 2012, 3, 2076-2081.
37. Beebe, J. M.; Kim, B.; Gadzuk, J. W.; Frisbie, C. D. Kushmerick, J. G. Transition from Direct Tunneling to Field Emission in Metal-Molecule-Metal Junctions. *Phys. Rev. Lett*. 2002, 97, 026801.
38. Yan, X. B.; Zhou, Z.; Ding, B.; Zhao, J.; Zhang, Y. Superior Resistive Switching Memory and Biological Synapse Properties Based on a Simple TiN/SiO 2/p-Si Tunneling Junction Structure. *J. Mater. Chem. C*. 2017, 5, 2259-2267.
39. Kim, S.; Jung, S.; Kim, M. H.; Cho, S.; Park, B. G. Resistive Switching Characteristics of Si3N4-based Resistive-Switching Random-Access Memory Cell with Tunnel Barrier for High Density Integration and Low-Power Applications. *Appl. Phys. Lett.* 2015, 106, 212106.
40. Yan, X. B.; Zhao, J.; Liu, S.; Zhou, Z.; Liu, Q.; Chen, J.; Liu, X. Y. Memristor with Ag-Cluster-Doped TiO_2 Films as Artificial Synapse for Neuroinspired Computing. *Adv. Funct. Mater*. 2018, 28, 1705320.

41. Pfister, J. P.; & Gerstner, W. Triplets of Spikes in a Model of Spike Timing-Dependent Plasticity. *J. Neurosci*., 2006, 26, 9673-9682.

42. Froemke, R. C.; & Dan, Y. (2002). Spike-Timing-Dependent Synaptic Modification Induced by Natural Spike Trains. *Nature*, 2002, 416, 433-438.

43. Wang, H. X.; Gerkin, R. C.; Nauen, D. W.; & Bi, G. Q. Coactivation and Timing-Dependent Integration of Synaptic Potentiation and Depression. *Nat. Neurosci*. 2005, 8, 187-193.

44. Yang, R.; Huang, H. M.; Hong, Q. H.; Yin, X. B.; Tan, Z. H.; Shi, T.; Zhou, Y. X.; Miao, X. S.; Wang, X. P.; Mi, S. B.; Jia, C. L.; Jia, C. L. Synaptic Suppression Triplet-STDP Learning Rule Realized in Second-Order Memristor. *Adv. Funct. Mater*. 2018, 28, 1704455.

45. Wang, Z. Q.; Zeng, T.; Ren, Y. Y.; Lin, Y.; Xu, H.Y.; Zhao, X. N.; Liu, Y. C., & Ielmini, D. Toward a Generalized Bienenstock-Cooper-Munro Rule for Spatiotemporal Learning Via Triplet-STDP in Memristive Devices. *Nat. Commun*. 2020, 11, 1-10.

46. Ambrogio, S.; Ciocchini, N.; Laudato, M.; Milo, V.; Pirovano, A.; Fantini, P.; Ielmini, D. Unsupervised Learning by Spike Timing Dependent Plasticity in Phase Change Memory (PCM) Synapses. *Front. Neurosci-Switz*. 2016, 10, 56.

47. Hou, C., Xu, Z., Qiu, W., Wu, R., Wang, Y. Xu, Q., Liu, X. Y., Guo, W. A Biodegradable and Stretchable Protein-Based Sensor as Artificial Electronic Skin for Human Motion Detection. Small, 2019,15, 1805084.

48. Guo, C., Li, C., Kaplan, D. L., Enzymatic Degradation of Bombyx Mori Silk Materials: A Review. Biomacromolecules, 2020, 21,1678-1686.

49. Song, Y.; Lin, Z.; Kong, L.; Xing, Y.; Lin, N.; Zhang, Z. & Liu, X. Y. Meso-Functionalization of Silk Fibroin by Upconversion Fluorescence and Near Infrared In Vivo Biosensing. *Adv. Funct. Mater*. 2017, 27, 1700628.

50. Meng, D.; Zheng, B.; Lin, G.; & Sushko, M. L. Numerical Solution of 3D Poisson-Nernst-Planck Equations Coupled with Classical Density Functional Theory for Modeling Ion and Electron Transport in a Confined Environment. *arXiv preprint arXiv*:2014, 1407.0674.

Figure Captions

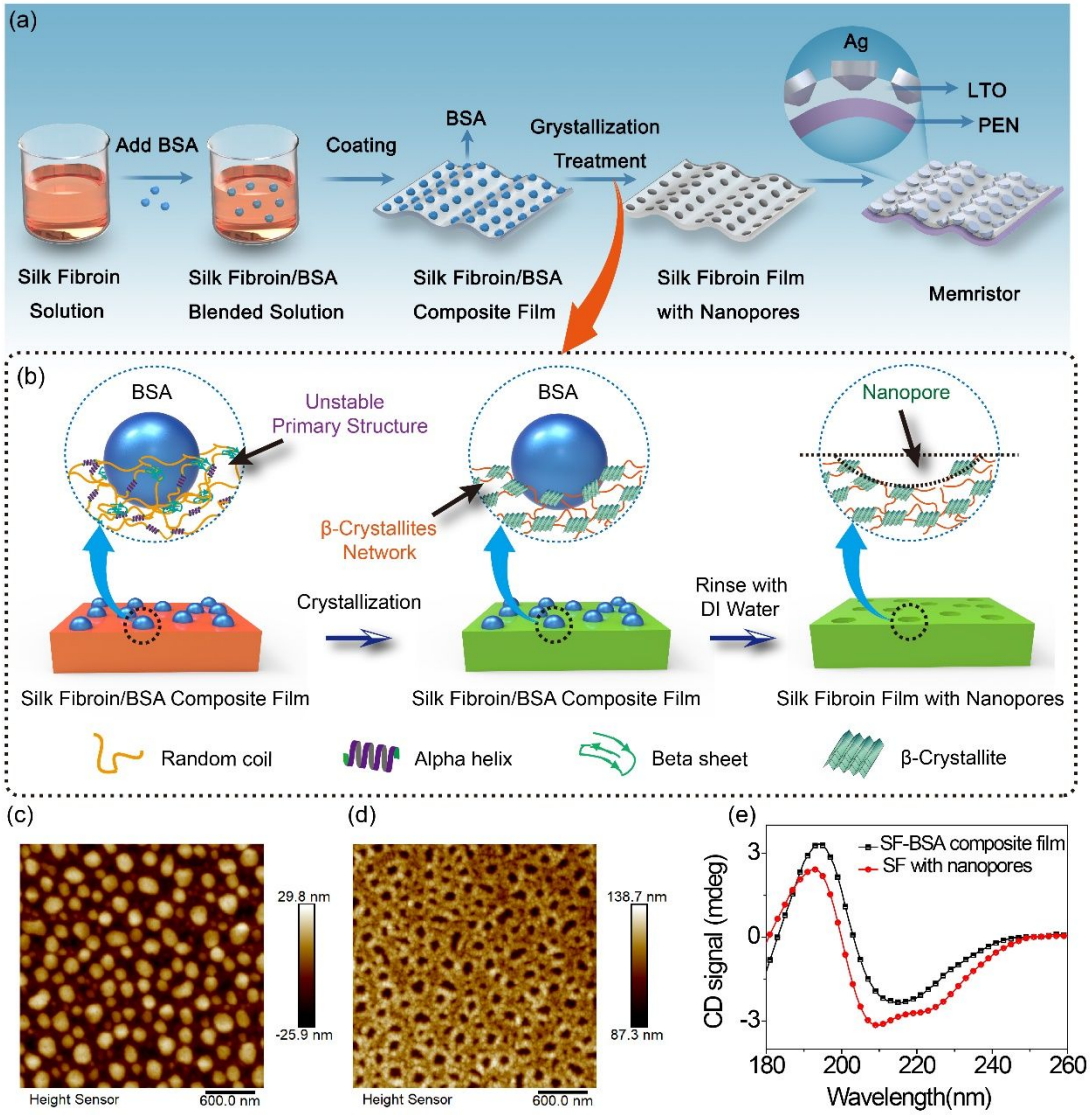

Figure 1. The fabrication process and structure analysis of p-SF film. (a) The fabrication process of p-SF film and schematic illustrations of memristor. BSA was taken as a porogen. The mass ratio of the obtained mixed solution is SF: BSA = 80: 20. (b) The diagram of BSA phase-separated on the meso-scale and formation of uniform aggregates in hybrid film. (c) Atomic force microscopy (AFM) images of the SF/BSA hybird film. (d) AFM image of the p-SF film. (e) Far-UV CD spectra of protein film. The positive peak at 194 and the negative peak at 217 nm are the characteristics of the structure of the β-sheet.

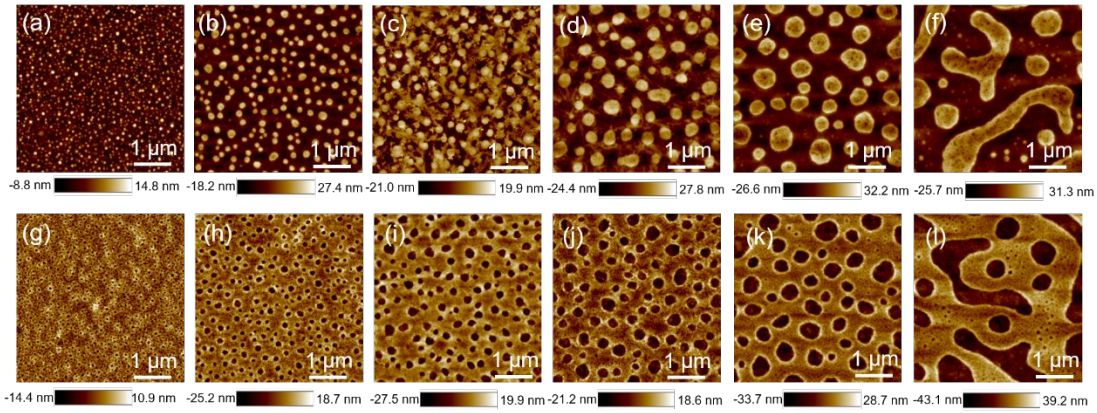

(A)

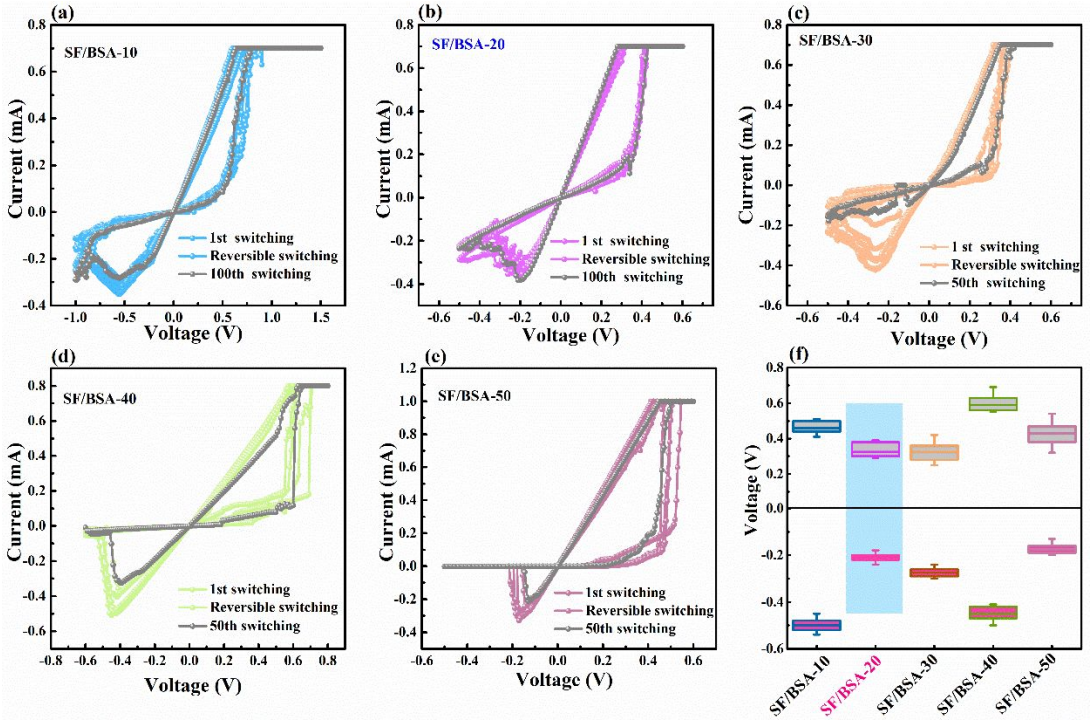

(B)

Figure 2. (A) The AFM image SF/BSA hybrid film. (a) p-SF-10 film; (b) p-SF-20 film; (c) p-SF-30 film; (d) p-SF-40 film; and (e) p-SF-50 film and (f) p-SF-60 film. The AFM image of porous SF film. (g) p-SF-10 film; (h) p-SF-20 film; (i) p-SF-30 film; (j) p-SF-40 film; and (k) p-SF-50 film and (l) p-SF-60 film. (B) I-V characteristic curve of SF/BSA hybrid film. (a) SF/BSA-10 film (b) SF/BSA-20 film (c) SF/BSA-30 film (d) SF/BSA-40 film (e) SF/BSA-50 film (f) On- and off-voltage statistics in different proportion. (B) I-V characteristic comparison of different ratios of BSA to SF. (a)-(e)Typical memory switching I–V curves. (f)The distribution of set voltage and reset voltage.

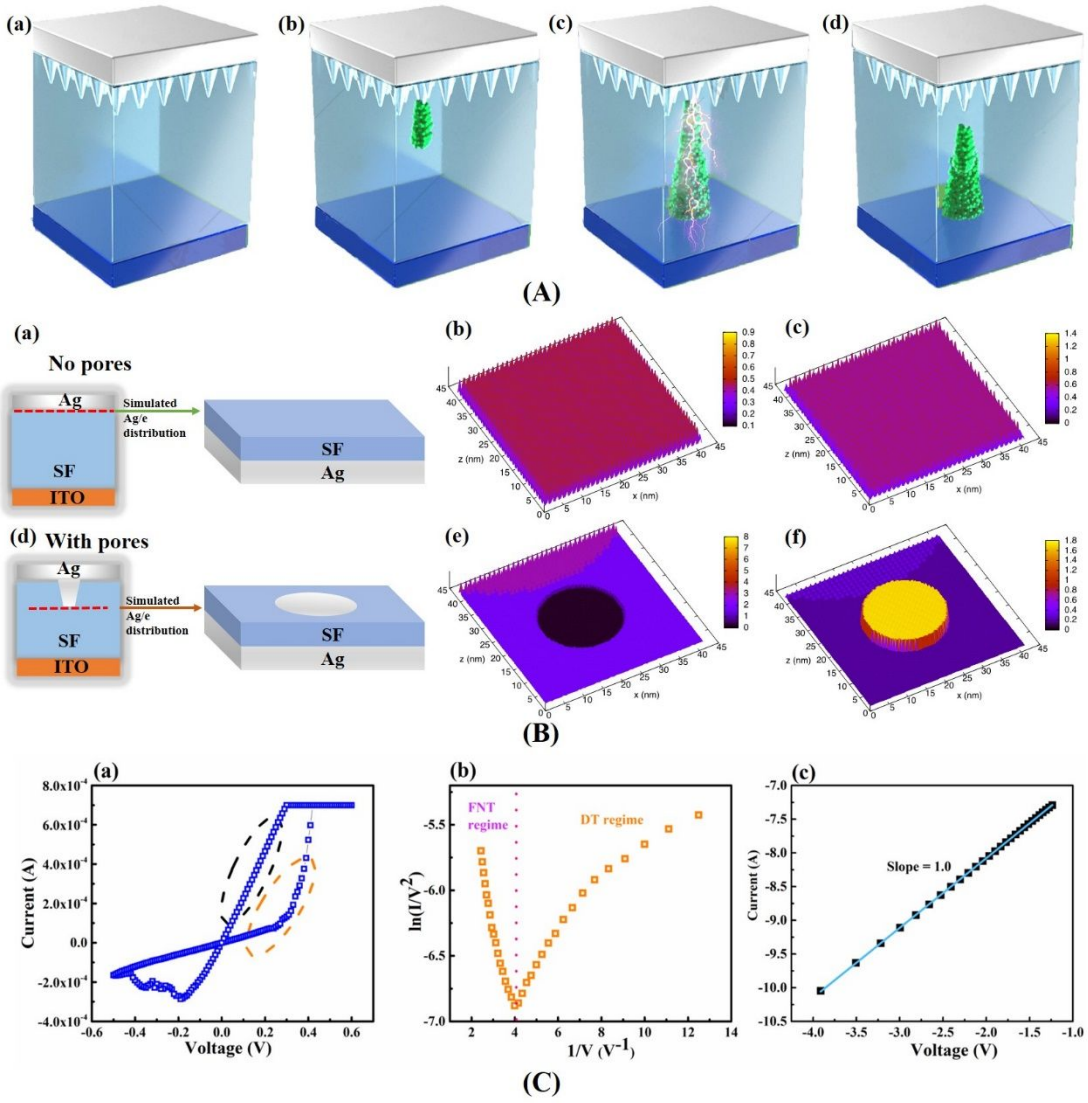

Figure 3. (A) Schematic of the conduction mechanism in the Ag/p-SF/ITO device. (a) Ag distribution in the Ag/p-SF/ITO device. (b) Conductive path formation in the HRS of the device. Ag ion moves from upper electrode to ITO electrode through p-SF film under positive voltage. (c) Conductive path formation in the LRS of the device. Reduction of Ag Ions to Ag Atoms on ITO Electrodes. (d) The Ag conductive filament breaks after applying negative voltage. (B) Ion and electron transport in silk fibroin memristor. Uniform ion and electron distribution are observed in the absence of nanopores in the SF layer (a-c) When nanopores are present, the spatial separation of ion and electron diffusion pathways is observed: Ag+ preferential diffuses through the pores and electrons through the SF network (d-f). The densities are given in M units. The electric field is applied to Ag electrode and the steady state distribution of (c), (f) Ag^{+} ions and (b), (e) electrons is plotted in the plane parallel to the Ag electrode / SF interface at the distance of 3 nm from the interface. (C) The mechanism analysis diagram of the device. (a) The I-V curve of Ag/p-SF/ITO devices. (b) Fitting curve

of I-V region data at HRS. The fitting results are divided into two parts, corresponding to direct tunneling (DT) and FN tunneling in low and high electric fields respectively. (c) The conduction mechanism analysis of I-V curve at ON-states. The red region of the I-V curve corresponds to the ohmic contact with a slope of 1.

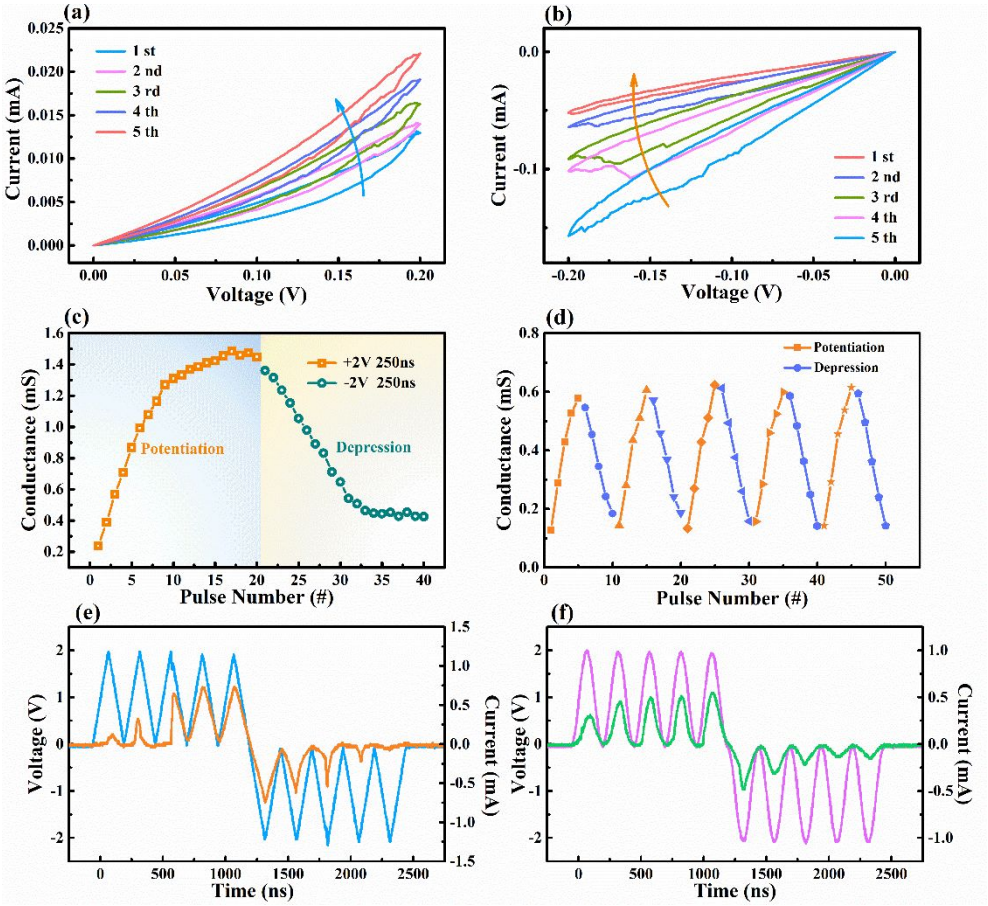

Figure 4. (a) and (b) *I–V* characteristics of the memristor under positive and negative bias voltages, respectively. The voltage is scanned from zero to 0.2 (-0.2) V and then returned to zero. (c) By applying continuous enhancement (suppression) pulses, the conductivity of memory can be improved (decreased). (d) The repetitive characteristics of conductivity modulation. The potentiation and depression of conductance are maintained by alternating positive and negative pulses. (e) and (f) Time variations of voltage and current under triangular and sine-wave applied voltages, respectively. In (f), the applied voltage is $\pm v_0 \sin^2(\omega_0 t)$, where v_0 is the magnitude (2 V) of the applied voltage and ω_0 is the frequency (4 MHz). The colors of the plots in (e) and (f) indicate the applied voltage and the corresponding current responses of the pulse series (blue and orange respectively in (e); orange and green respectively in (f)).

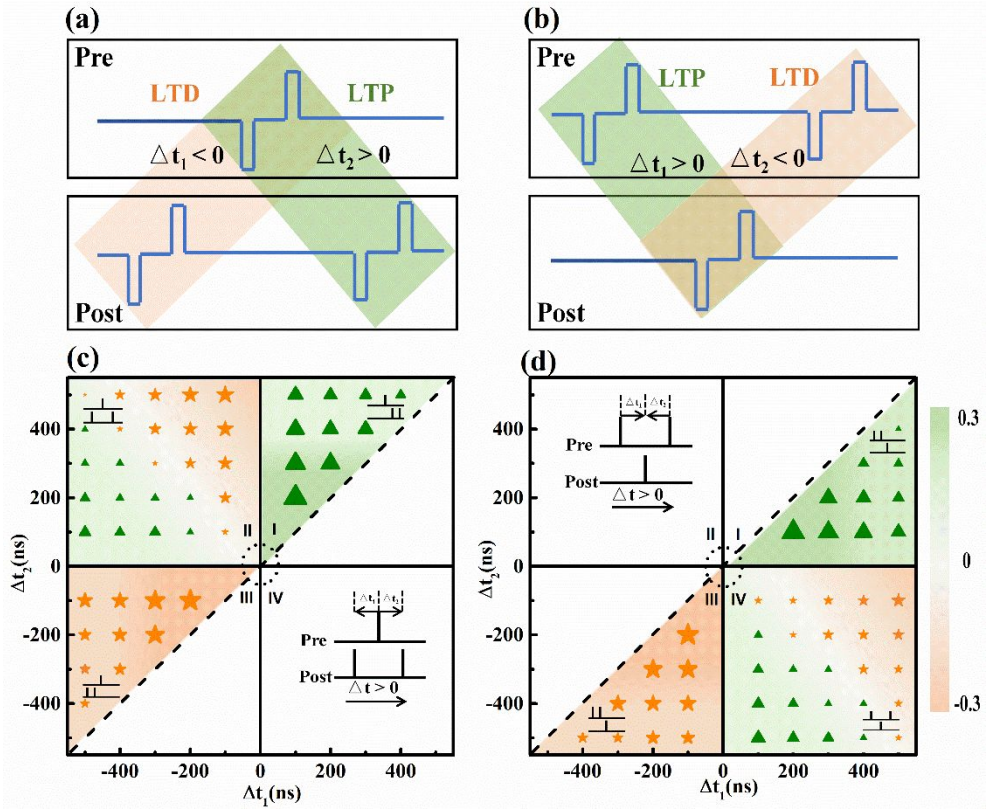

Figure 5. The schematic of the typical "post-pre-post" and "pre-post-pre" triplets. (a) post-pre-post: one pre-spike and two post-spikes (b) pre-post-pre: two pre-spikes and one post-spike. Each pre- or postsynaptic spike comprises two pulses with amplitude V_+/V_- =1 V/−1 V and duration 100ns. (c)-(d) All the experimental data are obtained in one device with a middle conductance of 0.6 mS. The symbols are the experimental data. The color of the symbols indicates the sign of the weight modification: green triangle for LTP, and orange stars for LTD. The size of the symbols background color indicates the magnitude of the weight change.

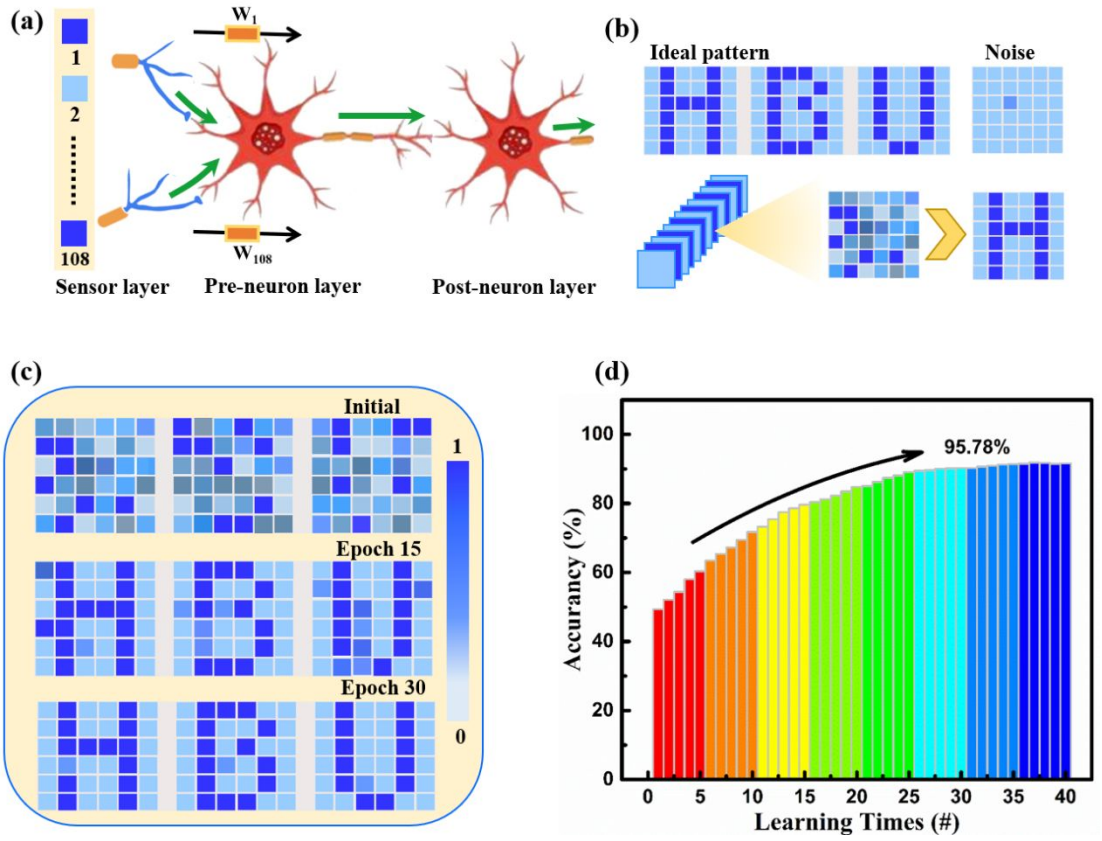

Figure 6. (a) Simulated neural network schematic diagram. The pre-neuron layer with 108 neurons is fully connected to one post-neuron through 108 memristor synapses with synaptic weight W_i. The pattern and random noise image are used to show the learning process. (b) Ideal learning patterns without noise and the noise pattern and the pre-neuron layer responds to pattern or noises and the mapping relationship of different layers. (c) Changes of synaptic weight map after learning different times under noise. The initial synaptic weights are randomly set. (d) The learning accuracy increases quickly with increasing times and then is saturated. Afterwards, the accuracy began to fluctuate around the saturation value.

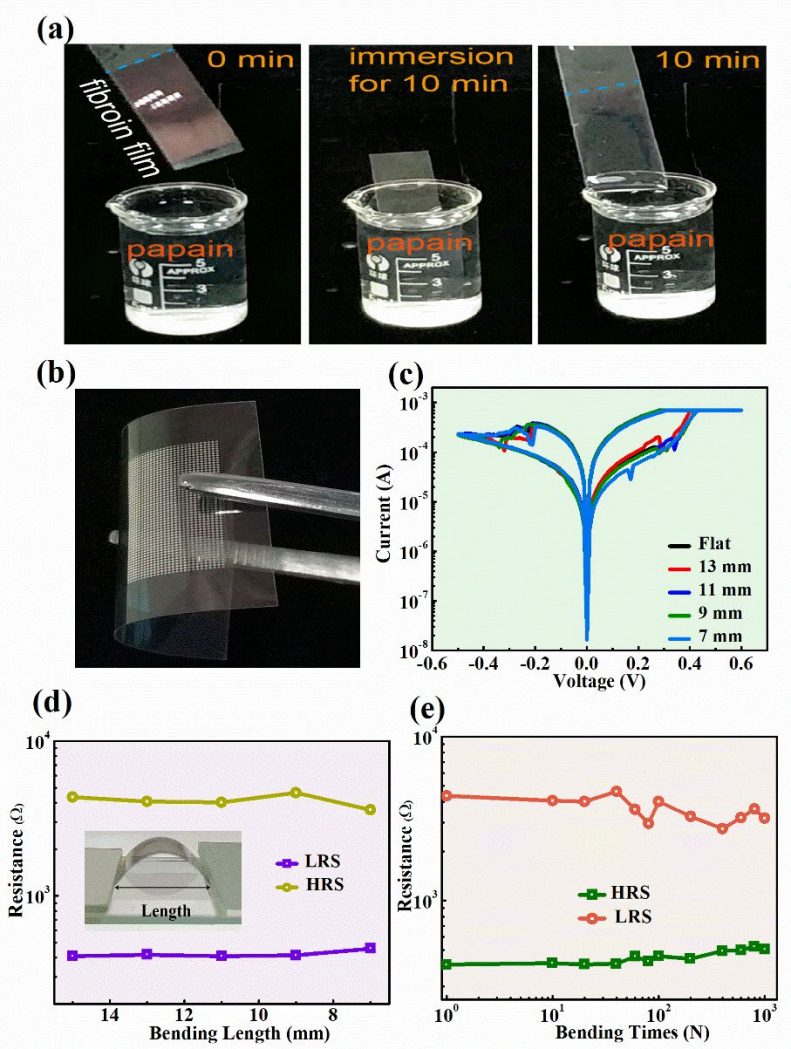

Figure 7. Degradation experiment of p-SF film memristor. (a) The dissolution process of p-SF memristor in papain aqus solution (0.5 mg mL^{-1}). The initial state of the p-SF memristor in papain solution can be seen and completely dissolved after 10 min. (b) Flexibility diagram of the memristor. (c) I-V curves with different bending radii. (d) Comparisons of HRS and LRS data with different bending length. (e) Comparisons of HRS and LRS data with different bending time.

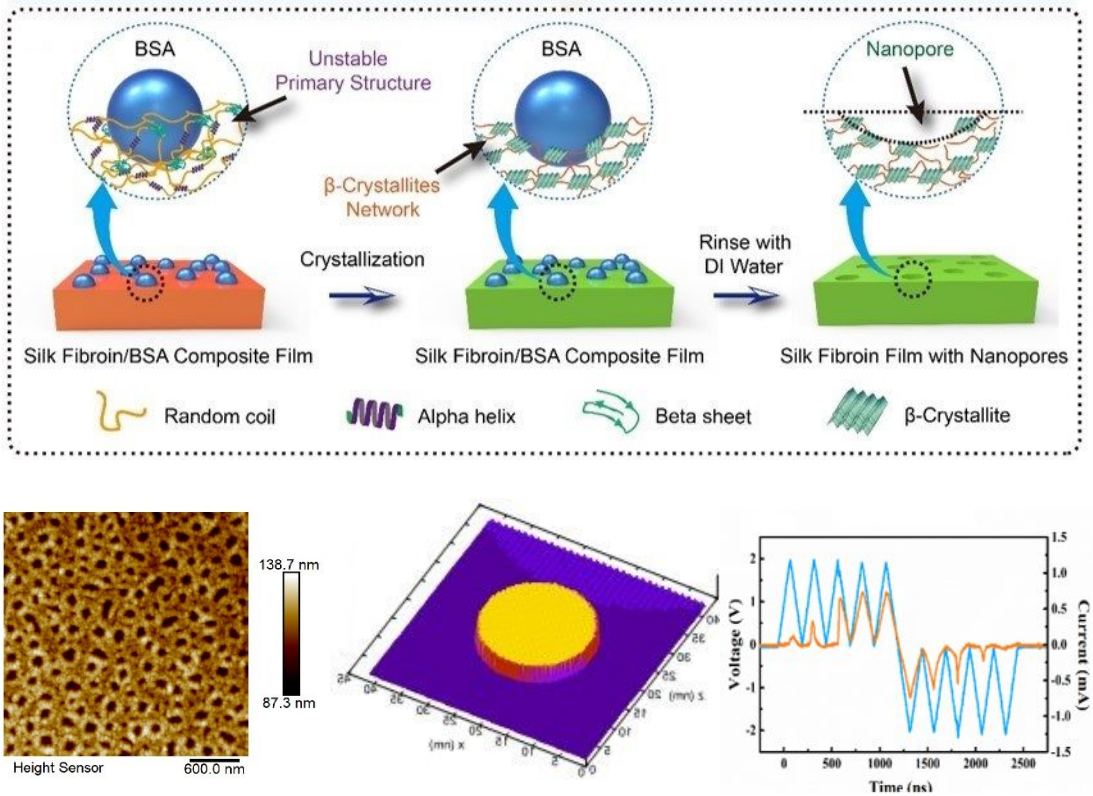

Graphic for manuscript